Research Article

Samira Elaissi*, Norah A.M. Alsaif, Eman M. Moneer and Soumaya Gouadria

Optimal conditions for indoor air purification using non-thermal Corona discharge electrostatic precipitator

https://doi.org/10.1515/phys-2025-0237
Received June 9, 2025; accepted October 4, 2025;
published online December 3, 2025

Abstract: Cold plasmas improve indoor air quality by reducing fine and ultrafine particles threatening human health. Electrostatic precipitator (ESP) uses non-thermal corona discharge connected to negative DC high voltage needles with grounded parallel plate collectors. In this paper, a simulation of an ESP model is performed using COMSOL Multiphysics software to study optimal conditions for indoor air purification. Numerical results of current voltage distribution display a great correlation with experimental data. The corona current density, potential, electric field strength and density of space charges are investigated. Various geometric and operating parameters are utilized to investigate the ultrafine particles removal efficiency. Moreover, the collection efficiency and migration velocity are discussed according to particle size. ESP performance is affected by number of discharging wires as well as electrode size and configuration. A 94 % efficiency rate of removing particles from 0.01 to 0.25 μm radius is achieved under optimal conditions (40 kV, 1 m/s inlet velocity, five needles). In hence, controlling airborne particles through electrostatic precipitator technology under these optimal conditions has been proven to be reliable to remove ultrafine particles.

Keywords: air sterilization; particle transport; secondary flow; collecting efficiency; performance level

Nomenclature

d_0 (m)	discharge wire diameter
s_y (m)	space between wire and plates
s_x (m)	space between wire and wire
N	number of corona electrodes
L (m)	collection plates length
H (m)	collecting plate height
φ_0 (V)	applied voltage on wires
Q ($m^3\ s^{-1}$)	air flow rate
T (K)	temperature of air
P (Pa)	pressure of air
ρ_p ($kg\ m^{-3}$)	particles density
ε_p ($C\ V^{-1}\ m^{-1}$)	particles' permittivity
ρ ($kg\ m^{-3}$)	gas density
d_p (m)	diameter of particles
$\vec{J}$ ($A\ m^{-2}$)	current density vector
D_i (m^2/s)	ion diffusion coefficient
$\vec{E}$ ($V\ m^{-1}$)	electric field vector
z_i	sign of the electric charge
ρ_i ($C\ m^{-3}$)	space charge density
$\vec{u}\ (u_x, u_y, u_x)$ ($m\ s^{-1}$)	fluid velocity vector
φ (V)	electric potential
ε_0 ($C\ V^{-1}\ m^{-1}$)	free space permittivity
μ_g (Pa s)	dynamic viscosity of the gas
$\overrightarrow{F_{EHD}}$ (N)	electrodynamic force vector
m_p (kg)	mass of particles
$\vec{u}_p$ ($V\ m^{-1}$)	particles' velocity
$\overrightarrow{F_c}$ (N)	electric force vector acting on particles
q_p (C)	particle charge
$\overrightarrow{F_d}$ (N)	drag force vector
τ_p (s)	response time of particle velocity
Re_r	relative Reynolds number
C_D	drag coefficient
C_S	Cunningham factor
λ (m)	molecule mean free path
S	coefficient of drag correction
C_1, C_2, C_3	constant coefficient specific to ESP shape and the flow regime
Kn	Knudsen number
υ_s	charge saturation of a particle
τ_c (s)	characteristic charging time
e (C)	elementary charge
K_B ($J\ K^{-1}$)	Boltzmann's constant
K_i (m^2/Vs)	ion mobility
E_s ($V\ m^{-1}$)	breakdown electric field

***Corresponding author: Samira Elaissi**, Department of Physics, College of Science, Princess Nourah Bint Abdulrahman University, P.O. Box 84428, Riyadh, 11671, Saudi Arabia, E-mail: saelaissi@pnu.edu.sa.
https://orcid.org/0000-0003-0149-9053
Norah A.M. Alsaif, **Eman M. Moneer and Soumaya Gouadria**, Department of Physics, College of Science, Princess Nourah Bint Abdulrahman University, P.O. Box 84428, Riyadh, 11671, Saudi Arabia.
https://orcid.org/0000-0001-7635-4719 (N. A. Alsaif).
https://orcid.org/0000-0002-2926-729X (S. Gouadria)

E_0 (V m^{-1})	corona discharge's onset electric field
r_0 (m)	corona wire radius
δ	relative number of gas density under standard conditions
P_s (Pa)	standard pressure
T_s (K)	standard temperature
P_L (Pa)	local pressure
T_L (K)	local temperature
p (W)	consumed total power
η (%)	particle collection efficiency
C_{outlet} (kg m^{-3})	particles' mass concentration at the outlet
C_{inlet} (kg m^{-3})	particles' mass concentration at the inlet
x (m)	particle size ranges
A (m^2)	collecting plate area in ESP
ω_p (m s^{-1})	particle's average migration velocity
$\vec{n}$	normal unit vector
p_c (W)	corona power ratio

1 Introduction

Air pollution is one of the major challenges the world faces today because of modern urbanization and industrialization [1]. There is a wide range of particle size range in indoor airborne particles, ranging from ultrafine particles (smaller than 0.1 μm) caused by cooking, smoking, burning candles/incense, and even household cleaning products to coarse particles (2.5 μm) that are caused by dust resuspension and outdoor infiltration (traffic and soil dust). It is crucial to consider particle size because smaller particles can reach deeper into the lungs, posing a greater risk to health. The risk associated with particles smaller than 10 μm is high since they are highly concentrated and can penetrate deep into the human body [2, 3]. Particles smaller than submicron such as aerosol particles penetrate the lungs, accumulating in the alveoli, and even infiltrating the blood [4].

As people from industrialized countries tend to spend most of their time inside, indoor transmission has been identified as the main setting for infections. Depending on their chemical composition, exposure time and intensity, these aerosols and airborne particles can cause respiratory and cardiovascular illness. Recently, these routes of transmission, contributed to the widespread of SARS-CoV-2 in indoor spaces [5, 6].

Indoor air pollution is reduced by a variety of processes, including, electret filtration hydrogenation [7], mechanical filtration and electrostatic precipitation (ESP). Conventional air filtration is considerably less expensive to operate and have a lower risk of damage and stoppage. However, these filters require change filters and may become bacterial sinks, causing high pressure drops as well [8]. An ESP is also easier to maintain than a filter since only collector plates need to be cleaned and there is no filter to be changed. Particles in the flow are ionized and transported by an electrical field [9]. ESP air purifiers generally achieve higher clean rate efficiency with nanoparticle collection than filters, because the velocity and flow rate of air delivery in discharge medium are higher than in fibrous media [10]. A significant advantage of ESPs is their ability to work. A wide range of gas temperatures can be handled, as well as high efficiency in collecting particles [11]. Their durability, cost effectiveness, and ease of operation make them a popular choice.

However, as there are several highly coupled processes in ESP, such as particle charging and migration in corona discharge, modelling these mechanisms remains challenging [12, 13].

There have been a number of numerical models developed to explore the characteristics of ESPs with respect to corona discharges and removal of polluted ultrafine particles. The advantages of numerical simulations over experimental studies are their flexibility, low cost, and relative accuracy. Modelling of the precipitation process using corona discharge is developed by Anagnostopoulos and Bergeles [14] with finite difference method to estimate wire surfaces' electric fields. To improve overcome some limitations of the previous model, Liu et al. [15] performed a simplified physical model, where particle motion and particle deposition onto electrodes are affected by electric field and space charge. However, this method has some flaws, including difficulty in assigning ion density at wire surfaces and difficulty handling special electrode geometries with high computational expense.

Furthermore, an investigation of particle charging models was conducted with a focus on their application to electrostatic precipitators [16, 17]. Also, particle behaviour effect is examined to determine its influence on particle collection by altering the electric field [18]. Recently, a rapid advancement in numerical technology has prompted many authors to model complex physical phenomena simultaneously with multiple software packages [19]. There are also several modifications of collection and discharge electrodes in ESPs to increase their collection efficiency, mainly for submicron particulate matter. Even though these designs need further investigation to confirm their effectiveness, which are often complex in structure.

In this study, a model simulating corona discharges and couple processes in an ESP are developed in the first part of this article using COMSOL Multiphysics software [20]. This model provides novel insights into the physical mechanisms of ESP and improves this process while increasing collection efficiency and lowering energy consumption. Secondly, a discussion of novel adjustments of the operational

performance of conventional ESPs are performed to enhance electrostatic pre-charging and electrostatic agglomeration. The third part of the article focuses on improving the collection efficiency of ESPs, specifically, using submicron particles that are difficult to remove by traditional methods. To evaluate ESP performance, optimal operating conditions are selected to increase nanoparticle collection efficiency and reduce pollution in indoor air environments.

2 Mechanism of air precipitator

A schematic diagram of a single stage electrostatic precipitator is displayed in Figure 1. The ultrafine particle charging system involves an electrode system consisting of high voltage DC source connected to thin wire electrodes and a grounded collecting electrodes system [21].

Electrodes are connected using air as a medium. When the ESP starts working through the effect of the corona, molecules of air between the electrodes become ionized, resulting in a lot of free electrons and ions. Through the ESP, polluted air passes then, free electrons collide with polluted particles between the electrodes. These particles become negatively charged due to attachment with free electrons and will be moved by the electric force toward positive collecting plates. Shaking intermittently removes polluted particles from the collecting plates.

Electrostatic precipitators (ESPs) require high voltage power, so safety concerns are addressed through strict protocols, training, and technological advancements. These include lock-out/tag-out procedures, specialized management programs, the maintenance of insulators, and the development of dielectric-coated ESPs that are safer and more efficient at lower voltages.

It is possible that this high voltage level will cause some other reactions as well, such as the generation of ozone. Nevertheless, smaller particles have a higher mobility and are more easily attracted to lower charge levels. Furthermore, small particles can deposit electrostatically at a faster rate than they can diffuse or gravitate [22].

Due to their high efficiency in capturing even very fine particles and the ability to integrate into existing air handling systems, electrostatic precipitators (ESP) are largely used in real-world applications, including power plants, chemical factories, and medical settings [23].

The performance of ESPs can be affected by factors such as dust loading, corrosive gases, and fluctuating operating conditions, despite their inherent durability and efficiency. In order to maintain long-term stability, an ESP must be continuously monitored for performance and periodically maintained, including cleaning collection plates as particle buildup reduces efficiency. The design of modern ESPs incorporates automated control systems, non-metallic materials, and water film cleaning for long-term stability [24].

3 Numerical model

The numerical model is based on a two-dimensional (2D) single channel wire plate, which reduces the computational cost compared to 3D models. Consequently, faster iterations are possible in designing and optimizing ESP parameters like electric field distribution, particle trajectory, and overall efficiency while using less energy.

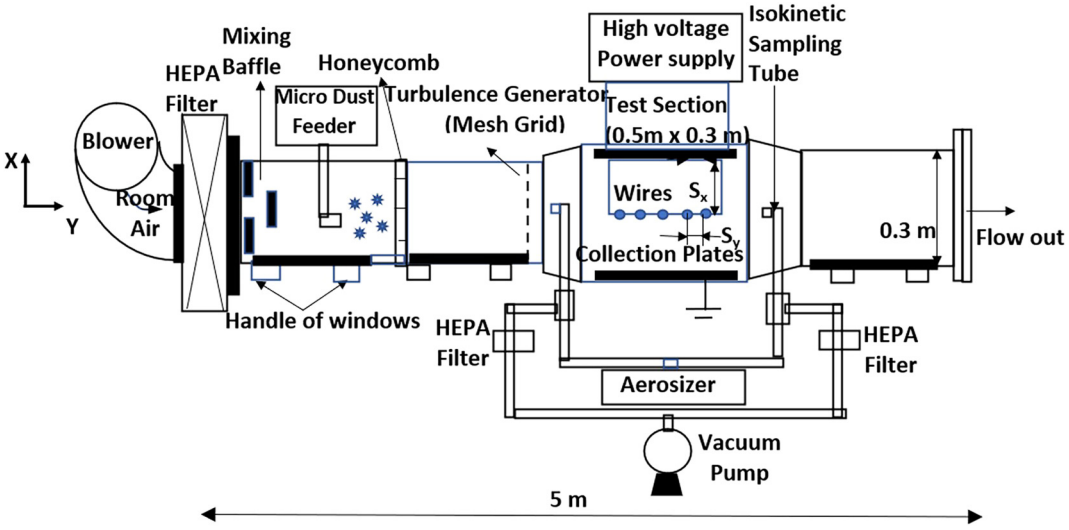

Figure 1: Schematic diagram of the laboratory single stage ESP.

Also, when modeling electrostatic precipitators (ESPs), constant air density and viscosity are often used, especially for small pressure drops and near-steady conditions. In some cases, these assumptions may be less accurate due to temperature variations or high particle loads, which can significantly affect performance. However, treating air as an incompressible Newtonian fluid makes modeling computationally efficient. In addition, ESPs are typically featuring with turbulent flow, where particles are chaotically arranged in three dimensions with eddies. However, using laminar flow can improve ESP performance, especially for sub-micron particulates, by enhancing particle collection on plates. Laminar flow can be achieved by controlling the vertical orientation of the housing and the downward direction of the gas in ESPs designed for fine particle removal.

Table 1: Operating conditions of the ESP.

Parameter, unit	Values
Diameter of discharge wire d_0 (mm)	1–3
Wire – plates distance s_y (mm)	50–200
Wire – wire distance, s_x (mm)	100–240
Number of corona electrodes N	3–8
Collection plates length L (mm)	700–960
Collecting plate height H (mm)	100–400
Applied voltage on wires, φ_0 (kV)	20–120
Inlet flow velocity, u_x (m/s)	1
Air flow rate Q (L/min)	50–150
Temperature of air, T (K)	293–500
Pressure of air, P (atm)	1
Particles density ρ_p (kg m^{-3})	2100
Permittivity of particles ε_p (C V^{-1} m^{-1})	10
Gas density ρ (kg m^{-3})	1.293
Diameter of particles d_p (μm)	0.01–10

3.1 Geometry model

As shown in Figure 2, ESP consists of five circular corona wires and two flat collecting plates [25]. Computational geometry model consists of a rectangle with a 0.7 m length and 0.1 m width, with five electrodes each having a 1 mm channel diameter. Duct inlet to first wire distance is 150 mm. 0.05 m is the wire-plate distance and 0.1 m is the distance between two wires. The operating conditions and dimensions are illustrated in Table 1.

There are four subprocesses in the theoretical analysis, each with its own governing equation, and the subprocesses interact with each other: particle dynamics model, particle charging, corona discharge, and gas flow model.

3.2 Corona model

With the simplified model of the corona, Poisson's equation combined with the charge conservation equations are used to solve the charge carrier transport. The transport of the charge carrier includes drift in the electric field and convection [26].

The current continuity equation:

$$\nabla \cdot \vec{J} = 0 \tag{1}$$

$$\vec{J} = \rho_i\left(z_i K_i \vec{E} + \vec{u}\right) - D_i \nabla \rho_i \tag{2}$$

$$\nabla^2 \varphi = -\frac{\rho_i}{\varepsilon_0} \tag{3}$$

$$\vec{E} = -\vec{\nabla}\varphi \tag{4}$$

Where $\vec{E}$ and $\vec{J}$ represent the electric field and the current density vectors respectively. z_i, ρ_i, D_i and K_i denote the sign of the electric charge, the density of space charge, the ion diffusion coefficient and the ion mobility respectively. $\vec{u}$ represents the fluid velocity vector, φ and ε_0 represent the potential and the free space permittivity.

As a result of manipulating these equations, the following equation for transport is obtained:

$$\mu\left(\frac{\rho_i^2}{\varepsilon_0} - \nabla\varphi \cdot \nabla\rho_i\right) + \nabla\rho_i \cdot \vec{u} = 0 \tag{5}$$

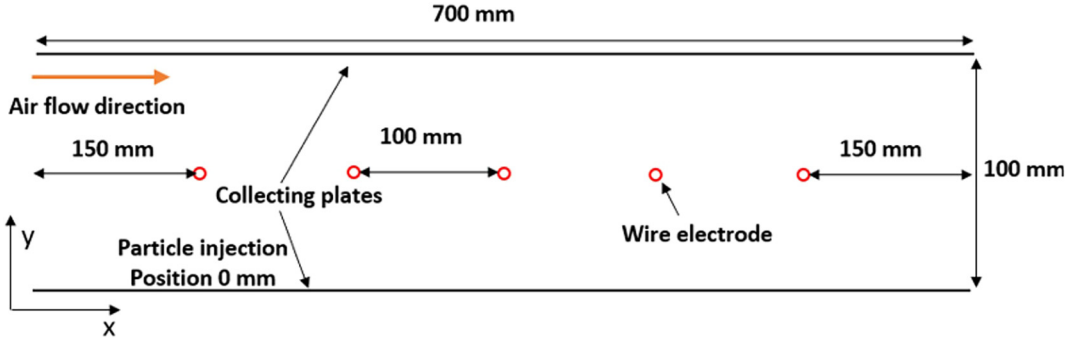

Figure 2: Modelled ESP geometry.

3.3 Gas flow

ESP dusty airflow is modelled as a compressible and steady-state laminar flow. The following equations are the gas flow's continuity and momentum [27].

$$\nabla(\rho\vec{u}) = 0 \tag{6}$$

$$\rho(\vec{u}\cdot\nabla)\vec{u} = \nabla\cdot\left[-P\cdot\vec{I} + \mu_g\left(\nabla\vec{u} + (\nabla\vec{u})^T\right)\right] + \overrightarrow{F_{\mathrm{EHD}}} \tag{7}$$

Here $\vec{u}$ represents the gas velocity vector. μ_g, ρ and P represent the dynamic viscosity, the fluid density and the pressure of the gas, respectively. $\overrightarrow{F_{\mathrm{EHD}}}$ represents the electrodynamic force defined as:

$$\overrightarrow{F_{\mathrm{EHD}}} = \rho_i\vec{E} \tag{8}$$

The main flow is affected by ionic wind in this equation.

3.4 Particle model

Lagrangian approach is used to track particle flow in the computational region up to the particle is trapped or ejected [28]. Due to the small order of magnitude of gravitational force and use of the two-dimensional model, particles are mostly influenced by electric force and aerodynamic drag force. Particle motion is expressed as follows:

$$\frac{\mathrm{d}(m_{\mathrm{p}}\overrightarrow{u_{\mathrm{p}}})}{\mathrm{d}t} = \overrightarrow{F_d} + \overrightarrow{F_c} \tag{9}$$

where m_{p} and $\overrightarrow{u_p}$ represent respectively, the mass, and the velocity of particles. $\overrightarrow{F_c}$ represents the electric force acting on these particles given by,

$$\overrightarrow{F_c} = q_p\vec{E} \tag{10}$$

where q_p is the particle charge. $\overrightarrow{F_d}$ denotes the drag force described with the model of Cunningham-Millikan-Davis [29].

$$\overrightarrow{F_d} = \frac{1}{\tau_p S}m_{\mathrm{p}}(\vec{u} - \overrightarrow{u_p}) \tag{11}$$

τ_p is the response time of particle velocity defined as

$$\tau_p = \frac{4\rho_p d_p^2}{3\mu_{\mathrm{g}}C_{\mathrm{D}}\mathrm{Re_r}} \tag{12}$$

S is the coefficient of drag correction given by:

$$S = 1 + \mathrm{Kn}\left(\mathrm{C}_1 + C_2\,\exp\left(\frac{C_3}{\mathrm{Kn}}\right)\right) \tag{13}$$

where, d_{p} and ρ_{p} are the diameter and the density of particles respectively. (C_1, C_2, C_3) are constant coefficients specific to ESP shape and the flow regime and Kn is the Knudsen number.

$\mathrm{Re_r}$ represents the relative Reynolds number:

$$\mathrm{Re_r} = \frac{\rho\vec{u} - \overrightarrow{u_{\mathrm{p}}}d_{\mathrm{p}}}{\mu_{\mathrm{g}}} \tag{14}$$

And C_{D} is the drag coefficient,

$$C_{\mathrm{D}} = \max\left[\frac{24}{C_{\mathrm{s}}\mathrm{Re_r}}\left(1 + 0.15\mathrm{Re_r^{0.687}}\right), 0.44\right] \tag{15}$$

In calculating drag forces, the Cunningham factor C_{S} is used to correct submicron particles whose size approach the molecular mean free path:

$$C_{\mathrm{S}} = 1 + \frac{2\lambda}{d_{\mathrm{p}}}\left[1.257 + 0.4\,\exp\left(-\frac{1.1\,d_{\mathrm{p}}}{2\lambda}\right)\right] \tag{16}$$

where λ represents the molecule mean free path [m].

Migration of particles is determined by particle charge. In an electrostatic precipitator, particles become charged through diffusion and field charging. Lawless model [30] provides the overall charging rate by combining the field charging velocity and the diffusion charge rate. When the particle charge is less than the saturated charge, the ions generated by corona discharge are accelerated by the field charge to collide with the particles to electrify them. On the contrary, the diffusion of ions produced by corona discharge due to thermal motion dominates:

$$\tau_c\frac{dq_{\mathrm{p}}}{dt} = \begin{cases} \dfrac{v_s}{4\varepsilon_0}\left(1 - \dfrac{v_e}{v_s}\right)^2 + \alpha & (v_e \le v_s) \\ \dfrac{(v_e - v_s)}{\exp(v_e - v_s) - 1}\alpha & (v_e > v_s) \end{cases} \tag{17}$$

τ_c is the characteristic charging time defined as [31]:

$$\tau_c = \frac{e}{4\pi\rho_i\mu_{\mathrm{g}}\mathrm{K_B}T} \tag{18}$$

And

$$v_e = \frac{q_{\mathrm{p}}e}{2\pi\varepsilon_0 d_{\mathrm{p}}\mathrm{K_B}T} \tag{19}$$

$$v_s = \left(3\omega_{\mathrm{e}}\frac{\varepsilon_{\mathrm{r,p}}}{\varepsilon_{\mathrm{r,p}} + 2}\right) \tag{20}$$

$$\alpha = \begin{cases} (\omega_{\mathrm{e}} + 0.475)^{-0.575} & (\omega_{\mathrm{e}} \ge 0.525) \\ 1 & (\omega_{\mathrm{e}} < 0.525) \end{cases} \tag{21}$$

$$\omega_{\mathrm{e}} = \frac{ed_{\mathrm{p}}}{2K_{\mathrm{B}}T}E \tag{22}$$

where, $\varepsilon_{\mathrm{r,p}}$ is the particle relative permittivity, e is the elementary charge, d_{p} is the particle diameter, τ_{c} is the characteristic charging time and K_{B} represents the Boltzmann constant. α and ω_{e} are the continuous constants of the model.

Table 2: Boundary conditions.

	Electric potential	Air flow	Particle transport	Charge density
Wire electrode	$-n\cdot\nabla\varphi = E_0\varphi = \varphi_0$	No-slip	Reflect	$\rho_q = \rho_0$
Collecting plates	$\varphi = 0$	No-slip	Freeze	$-n\cdot\nabla\rho_q = 0$
Inlet	$-n\cdot\nabla\varphi = 0$	$u_x = 1$ m/s$u_y = 0$ m/s	$u_x = 1$ m/s$u_y = 0$ m/s	$-n\cdot\nabla\rho_q = 0$
Outlet	$-n\cdot\nabla\varphi = 0$	Pressure outlet	Escape	$-n\cdot\nabla\rho_q = 0$

3.5 Boundary conditions

Table 2 displays the corresponding boundary conditions. There is a set value (φ_0) on the electrode wire surface and zero potential on the collecting plate. ESP inlet and outlet are also considered zero for the normal derivative of the potential.

Additionally, at the corona electrode, the normal component of electric field is used as the boundary condition for Poisson's equation.

$$\vec{n}\cdot\vec{E} = E_0 \tag{23}$$

In order to determine the density of space charges ρ_0 at the wire electrode, the imposed potential φ_0 is verified using Lagrange multiplier.

$$\vec{n}\cdot\vec{E} = E_0 \tag{24}$$

At the corona electrode, both potential and electric field are imposed in the model. The electric field value at the wire must be close enough to the real one to obtain predictive physical results. Peek's law is therefore applied [32]:

$$E_s = E_0\left(\delta + 0.03\sqrt{\frac{\delta}{r_0}}\right) \tag{25}$$

where E_s represents the breakdown electric field, E_0 is equal to 3×10^6 V/m, r_0 denotes the corona wire radius and δ represents the relative number of gas density under standard conditions.

$$\delta = \frac{T_s P_L}{P_s T_L} \tag{26}$$

where P_s and T_s are equal to 101,325 Pa and 273.15 K respectively, while P_L and T_L represent respectively, local pressure and local temperature.

Furthermore, the corona power ratio (p_c) assesses the electrostatic precipitator's power consumption in a practical environment from an economical perspective defined by [33]:

$$p_c = \frac{p}{Q} \tag{27}$$

where p and Q refer to the consumed total power and the gas flow rate, respectively.

The particle collection efficiency η is calculated as [34]:

$$\eta = 1 - \frac{C_{outlet}(x)}{C_{inlet}(x)} \tag{28}$$

where C_{outlet} and C_{inlet} represent particle mass concentration at the outlet and at the inlet of the ESP, respectively. The particle size ranges are represented by x. The particle collection efficiency η is expressed using the Deutch Anderson formula:

$$\eta = 1 - e^{-\frac{A\omega_p}{Q}} \tag{29}$$

where A is the effective collecting plate area in ESP. Q represents the gas flow rate and ω_p represents the particle's average migration velocity defined as the speed of particles moving towards the collecting plates given by [35]:

$$\omega_p = \frac{Q}{A}\ln(1-\eta) \tag{30}$$

4 Computational procedure

An independent mesh study was performed on the COMSOL Multiphysics® numerical model to ensure precision and stability. Table 3 illustrates the number of elements and nodes according to five domain meshes. As depicted in Figure 3, the relative errors ε_{Rel}, of the current density, J_{Ground}, at the grounded plate of the collection electrode is illustrated. The relative errors, ε_{Rel} decreases from around 1.15–0 %. Balancing computational time and model performance, the third domain mesh quantity, is employed for the ESP model, resulting in an error of approximately 0.3 % [36].

Table 3: The number of elements and nodes according to five domain meshes.

D_{Mesh}	$n_{elements}$	n_{nodes}
1	10,490	96,128
2	15,578	142,753
3	19,735	180,847
4	23,535	215,669
5	28,840	264,283

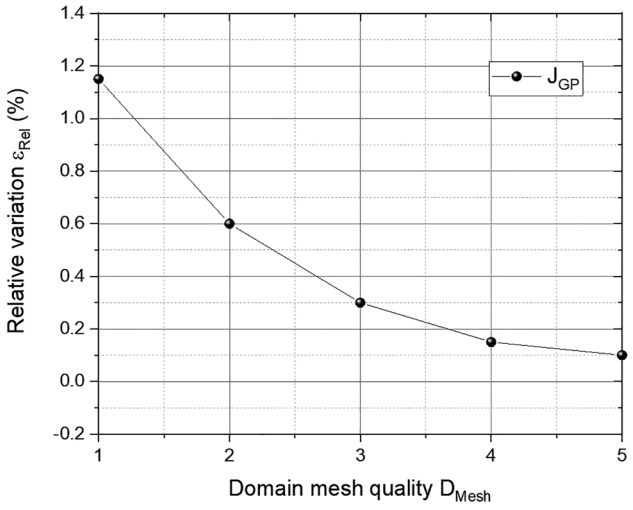

Figure 3: Distribution of the relative error ε_{Rel}, of the current density with domain mesh distribution.

It illustrates the accuracy of the grid at various locations without long computational time.

A dense grid is found close to the wire electrodes since, a high density of current region is developed around them. Figure 4 illustrates the unstructured triangular mesh using COMSOL Multiphysics software.

5 Results and discussion

An investigation of the wire plate ESP is conducted in this study using COMSOL Multiphysics Software. Simulated and experimental results are compared to assessing the model's validity. ESP performances are affected by various operational factors such as different electrodes and collecting plates are compared to determine their effects on air disinfection. In addition, the polluted particles removal efficiency and the migration velocity are investigated.

5.1 Characteristics current-voltage distribution

Numerical models for ESP were compared with experimental results. A comparison of the current-voltage relationship of an ESP at various interelectrode wire distance (Figure 5a) and different number of electrode discharge (Figure 5b) was made with those obtained experimentally by Kasdi [37]. In comparison with experimental data, the calculation error is less than 2 % and numerical results agree reasonably well with experimental results.

In Figure 5a, the model accurately predicts changes in corona current for different distances between wires. Corona current rises with higher interelectrode wire distance (s_x). As the wire spacing decreases, the shielding effect exerted by each wire increases causing the reducing of the discharge current. Current-voltage characteristics are shown in Figure 5b as a function of wire number. At the same voltage, as the number of discharging conductors (wire electrode) increasing, the current rises.

5.2 Current density distribution

As shown in Figure 6, the numerical simulation reveals the current density distribution on the dust collector's surface.

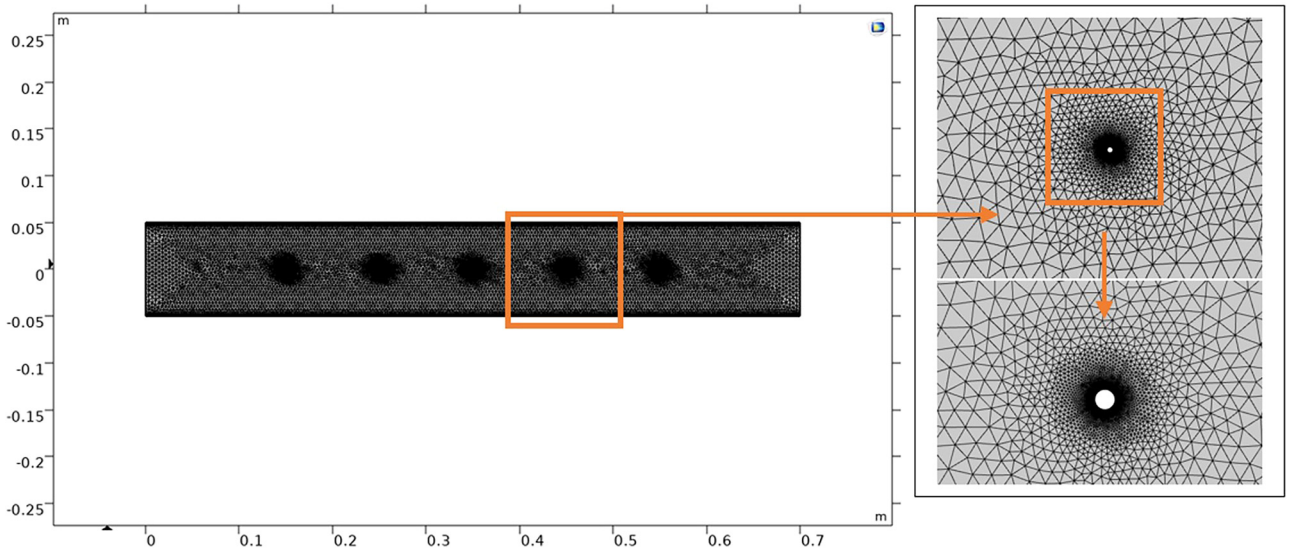

Figure 4: Modelled ESP geometry. Mesh picture of 2D ESP and refined mesh structure around wire electrodes.

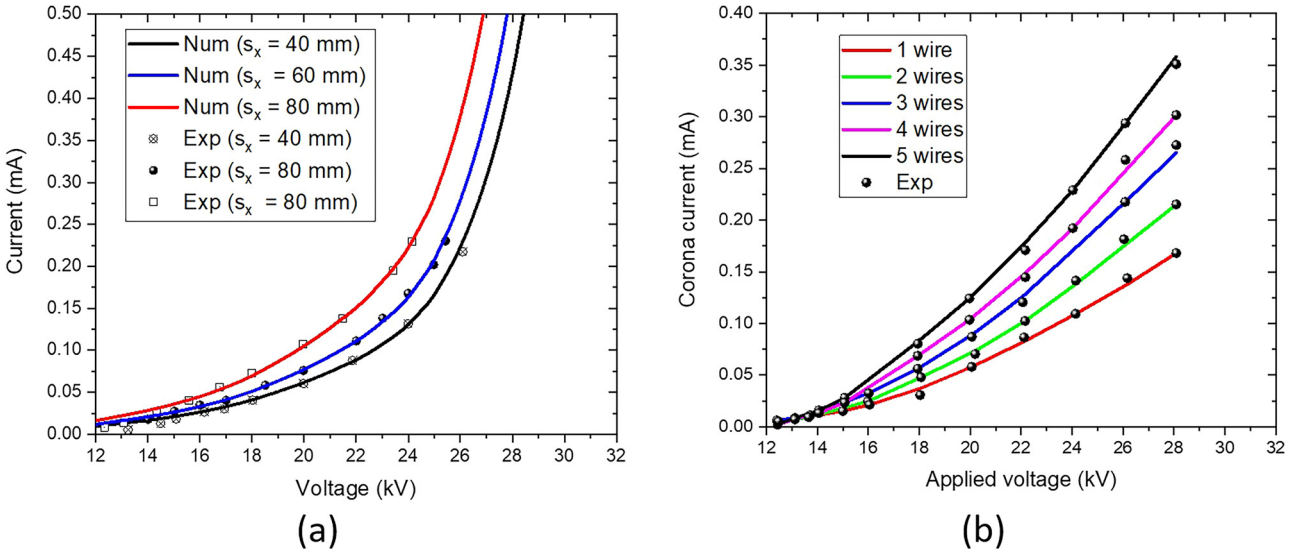

Figure 5: Comparison with simulated corona current-voltage characteristics and experimental date for (a) different wire spacing and (b) different number of wires.

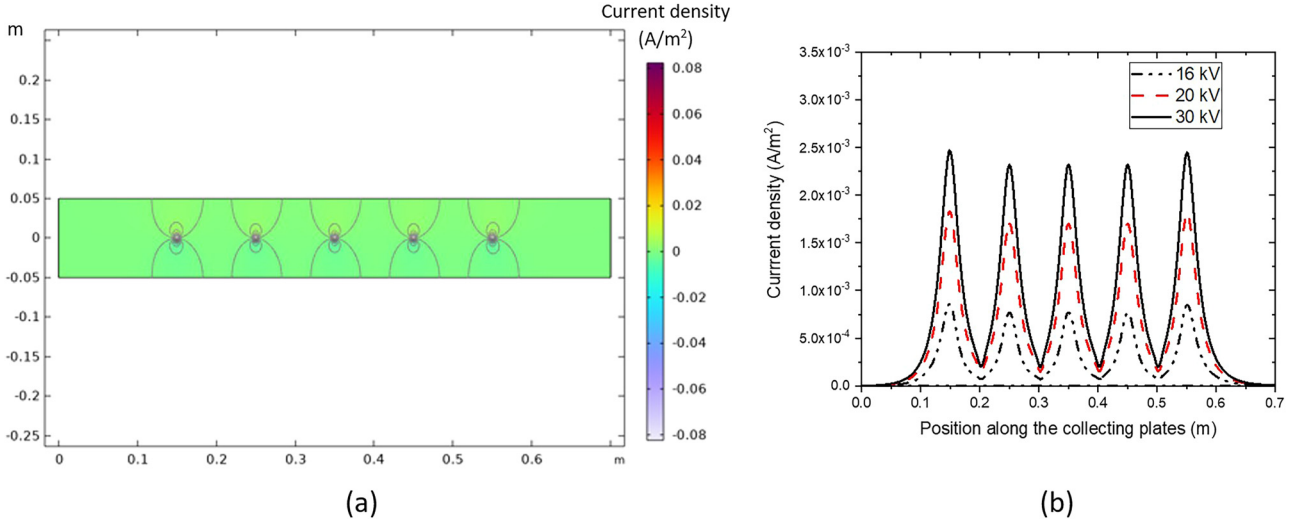

Figure 6: Current density: (a) 2D distribution, (b) linear distribution ($Y = 0.02$ m) at different voltage of wire electrode.

The current density displays a wave pattern along the collecting plate, with higher values under each wire and lower values between two neighbouring wires (see Figure 6a). At the end of all wire arrangements, there is a symmetrical peak of current density. Figure 6b shows that with increasing voltage, corona's current density increases and the electrostatic shielding degree (the ratio between the outer and inner discharge electrode) decreases. A stronger electrostatic shield is present at low voltages, while a weaker shielding occurs at higher voltage, increasing the current density.

5.3 Potential and electric field distribution

Figure 7 shows the distribution of electric potential in ESP. Figure 7a illustrates that there is a high electric potential near the discharge wire and a lower potential between two electrode wires. The applied potential at the wire electrode drops with decreasing radius values of electrode wire (see Figure 7b).

An electrostatic precipitator's electric field distribution is displayed in Figure 8. A high electric field appears near the discharge electrode, reaching a maximum of 7.6×10^6 V/m. A

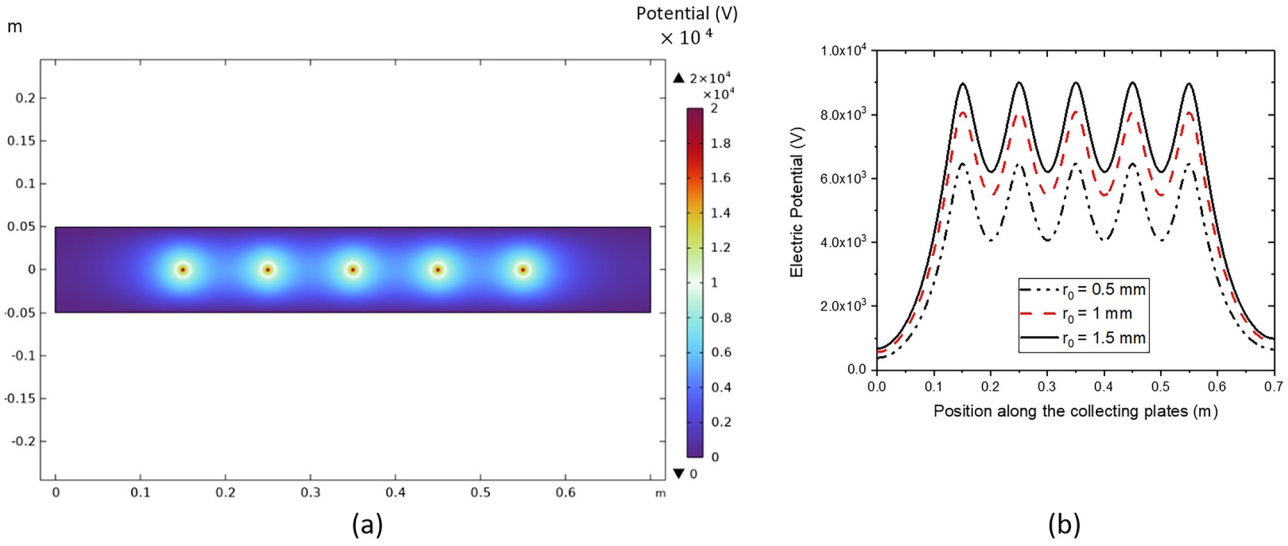

Figure 7: Electric potential: (a) 2D distribution, (b) linear distribution ($Y = 0.02$ m) at different wire electrode radius.

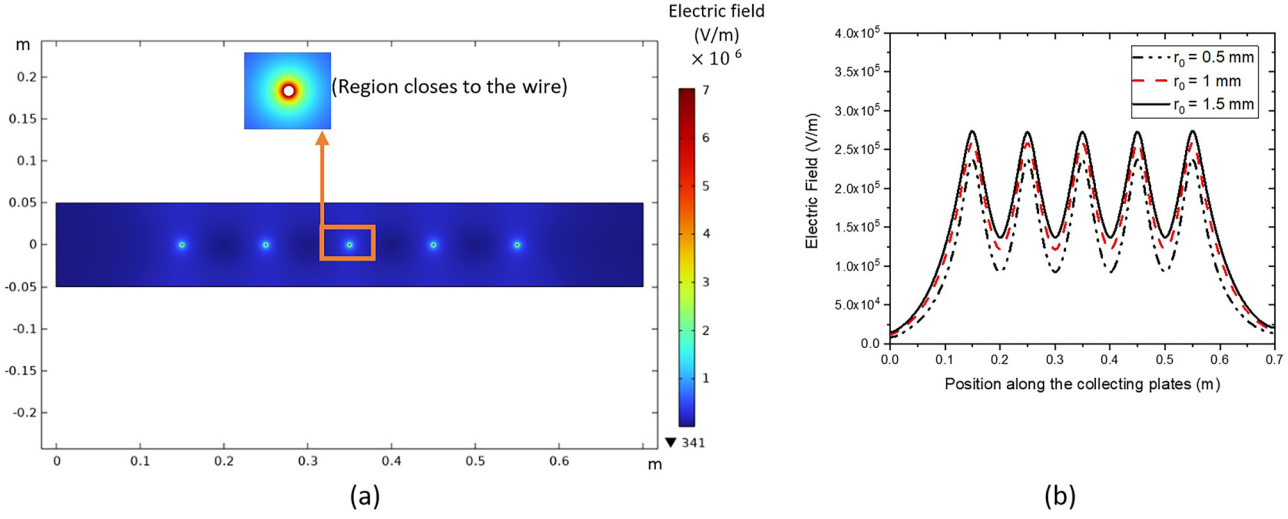

Figure 8: Electric field: (a) 2D distribution, (b) linear distribution ($Y = 0.02$ m) at different wire electrode radius.

high electric field strength region gradually extends during the rapid reduction of the electric potential into the collecting plates. The same polarity of the two neighbouring wires results in a reduced electric field area, lower than 102 Vm^{-1} (see Figure 8a).

The effect of discharge radius on corona discharge is studied by simulating ESP with five discharge electrodes at 20 kV applied voltage for three radii of the wires, namely 0.5, 1 and 1.5 mm. As displayed in Figure 8b, the electric field of five wires to ESP increase with rising radius of the active electrode.

5.4 Space charge density distribution

In Figure 9, the high space charge density near the inner electrodes exhibits a luminous corona discharge. Charge accumulation near the inner electrodes is accelerated by the combination of high space charge densities and intense electric fields. A decrease in space charge density occurred away from the discharge electrode as well as between two adjacent wires because of corona suppression (see Figure 9a).

Figure 9b shows that for 3 different radius values of electrode wire, the higher density area near the wire at

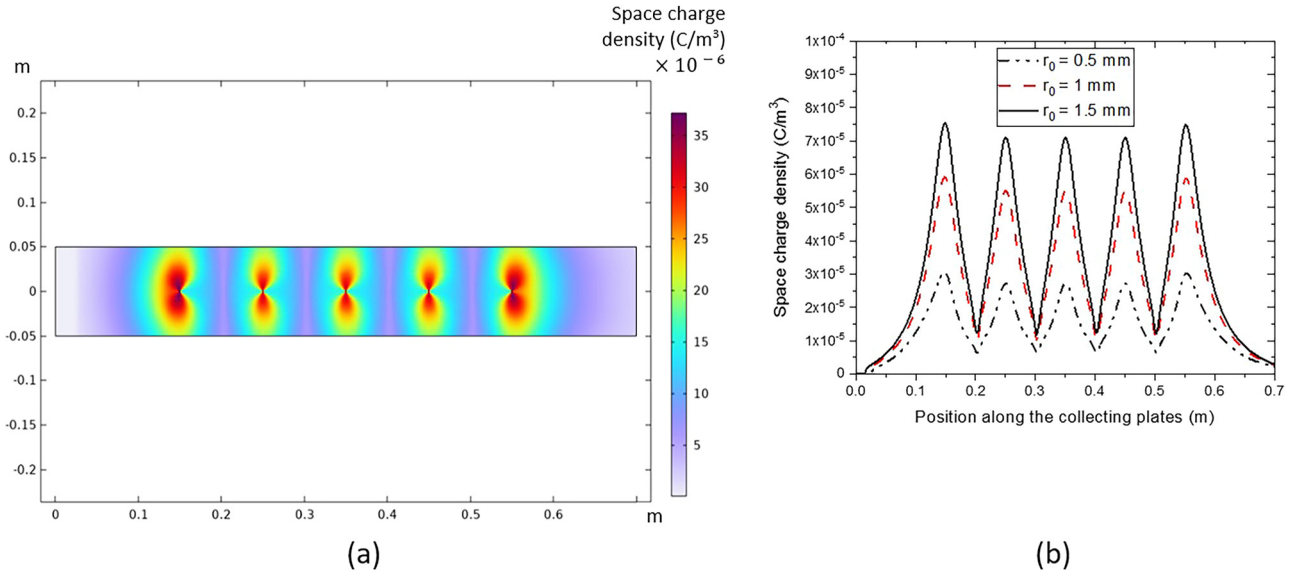

Figure 9: Space charge density: (a) 2D distribution, (b) linear distribution ($Y = 0.02$ m) at different wire electrode radius.

1.5 mm radius decreased with electrode size reduction. With 0.5 mm radius size, the peak value decreased by 80 %. Between the wires, there is a widening of the low-density region, with the lowest density near 0.

5.5 Characteristics of flow field

The gas velocity contours in the ESP are shown in Figure 10a. A strong volumetric force is introduced by combining high field strength with high ion charge density, resulting in an electro-aerodynamic secondary flow. A secondary stream, produced by ions motion, namely ionic wind, occurs in space due to the presence of the electrostatic field in the flow field. The discharge generates ionic wind that accelerates downstream flow, causing a reduction in local static pressure and a y-direction pressure difference. Thus, a local reverse flow occurs when fluid flows towards a wire.

Figure 10b illustrates the linear distribution of the velocity field along x axis associated with strength of the wind in the computational region. The minus y-component flow means the reverse flow. As electrode radius decreased from 1.5 to 0.5 mm, approximately 60 % of the speed difference between upstream and downstream of the wire is decreased, reducing the effect of ionic wind on gas flow. Furthermore, this decrease indicates that corona suppression restricts the motion of ions.

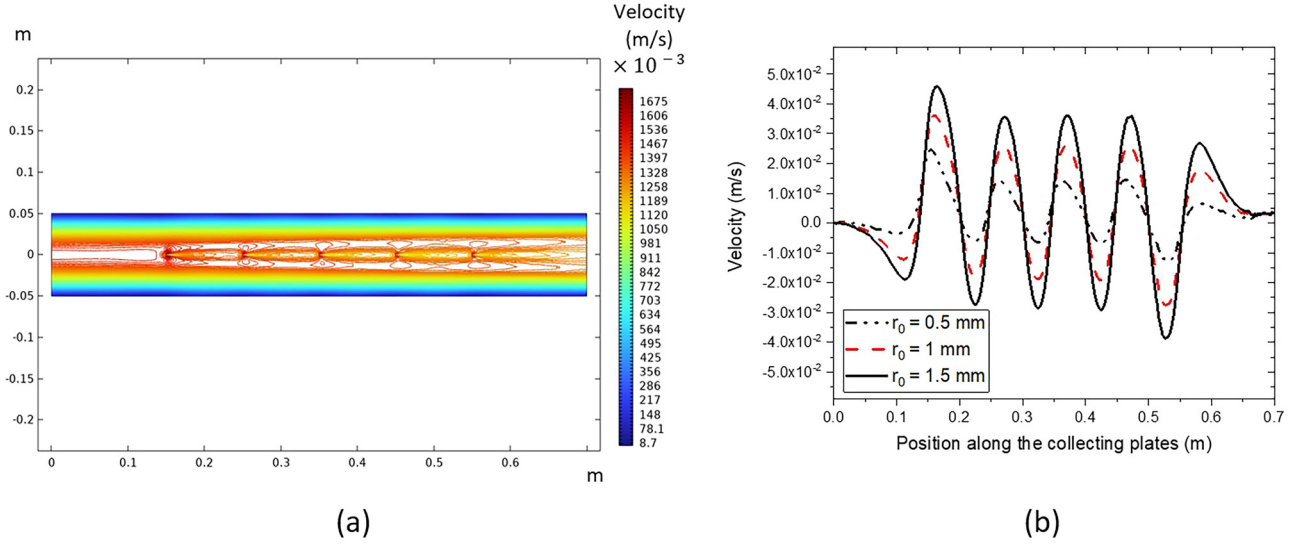

Figure 10: Flow velocity in the electrostatic precipitator: (a) 2D distribution, (b) linear distribution ($Y = 0.02$ m) at different wire electrode radius.

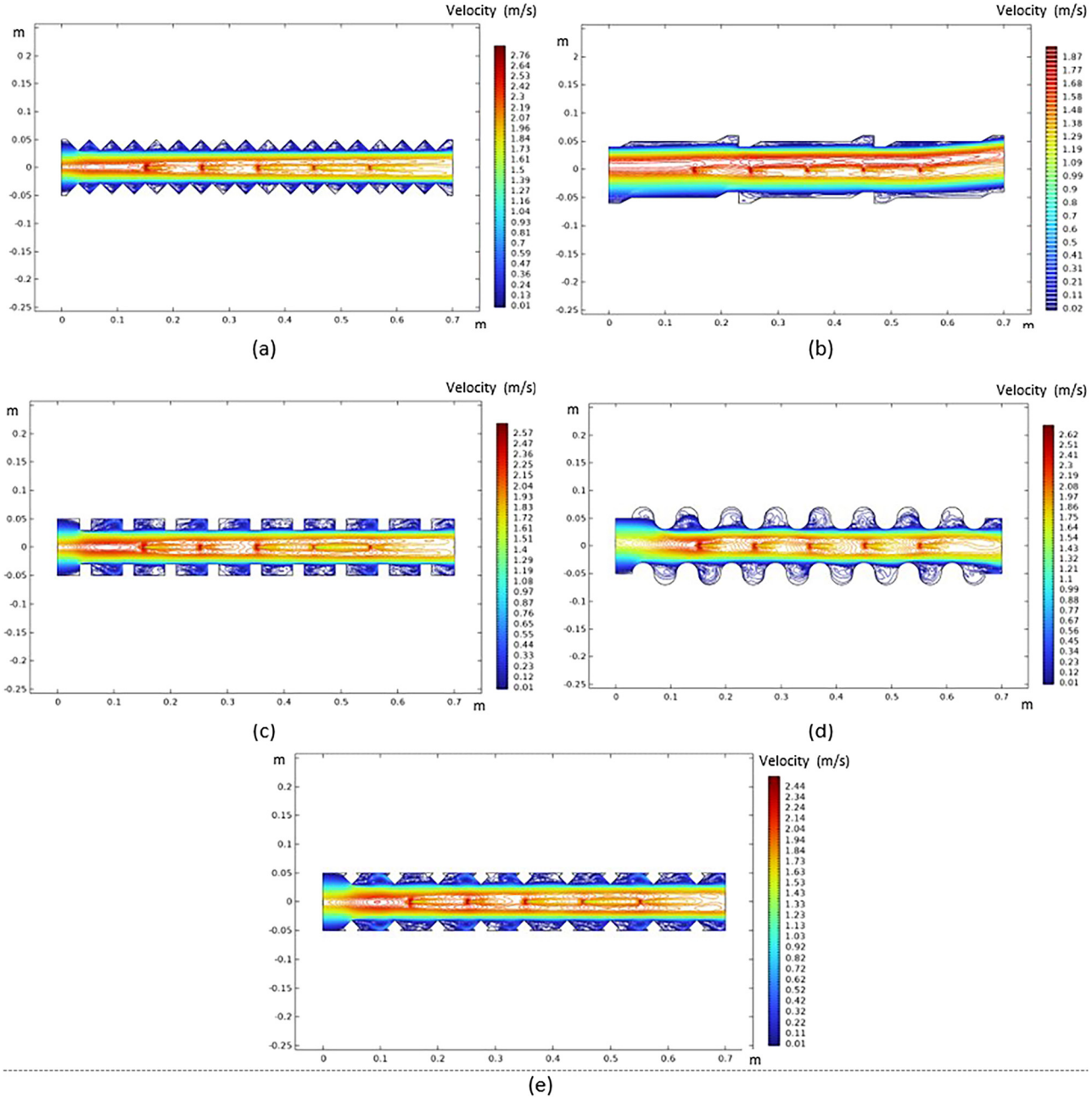

Figure 11: The air flow velocity distribution in ESP with (a) triangular plates, (b) BE-plates, (c) crenelated, (d) C-type and (e) corrugated collecting electrode with $u = 1$ m/s.

As illustrated in Figure 11, various shapes of collecting plates result in different distributions of velocity of flow in ESP. Around the wires, flow velocities reach between 1.6 and 1.8 m/s. Furthermore, with non-flat plates, the flow velocity decline significantly at $y = 50$ mm and attains 0.1 m/s but remains greater than those with flat plates in the ESP. Consequently, triangular collecting electrodes have the strongest impact on the reduction of re-entrainment effects and thus the improvement of dust removal efficiency. In the computational region, ionic wind generates a y-component velocity, and its strength is determined by the magnitude.

5.6 Particle charging and trajectory

Ultrafine particles' trajectory in an electrostatic field is influenced by a variety of forces, most notably, the drag force and the Coulomb force. Also, the particle size radius affects

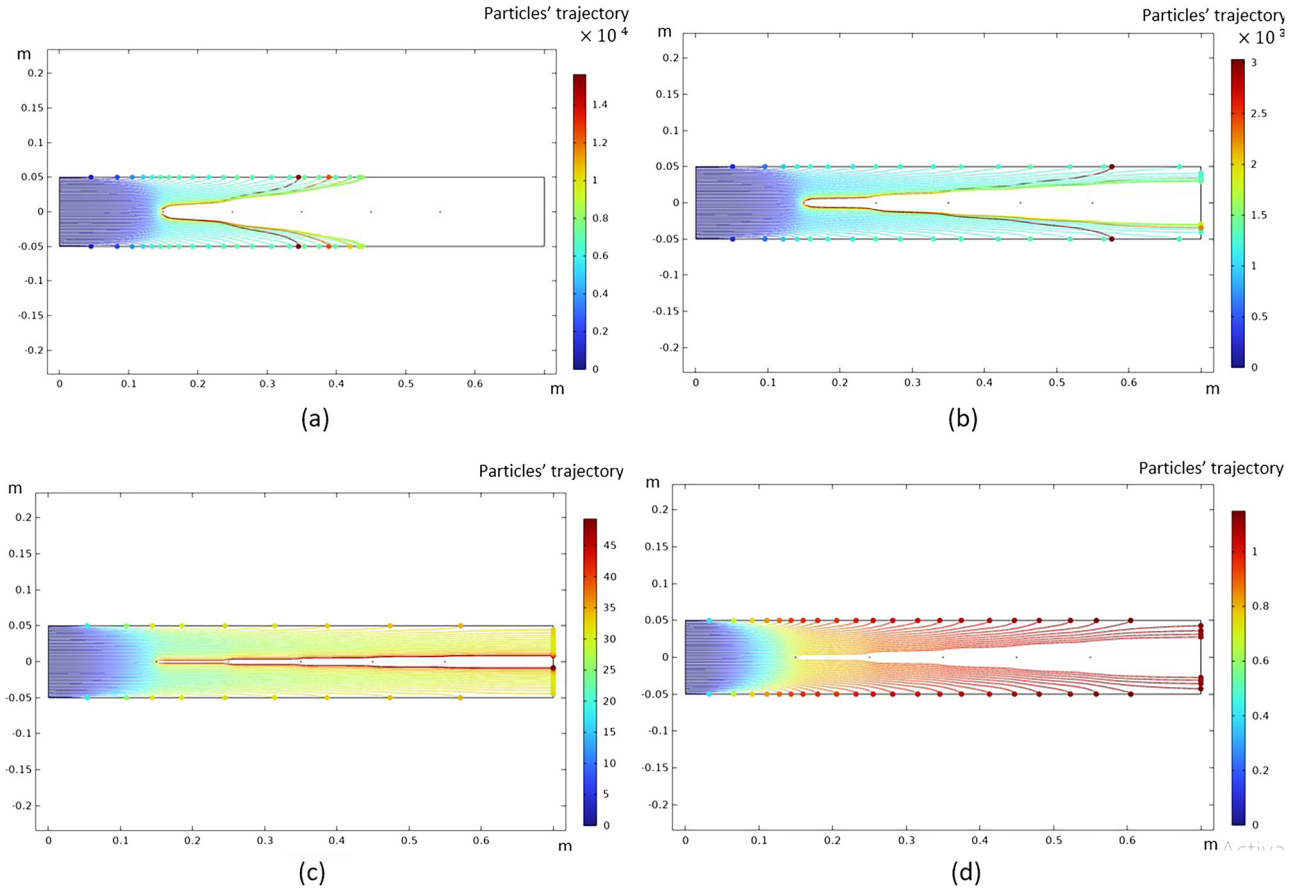

Figure 12: Particle trajectories with the charge number along the trajectory expressed in colour for different particles radius of (a – 5 µm, b – 2 µm, c – 0.2 µm, and d – 0.01 µm).

the motion of particles and the efficiency of dust particles collection by balancing drag and electric force.

In Figure 12, particles trajectories are illustrated for several particle's radius (r_p = 0.01–5 µm). After being released on the left, particles are carried by fluid flow transport in the direction of the right outlet. As the particles move along their trajectory, they become increasingly charged, resulting in an electric force that deviate their path in the direction of the wall.

With (r_p = 5 µm) particle's radius and in the ($0 < x < 0.1$ m) region, the electric field has little effect on the particle's trajectories, thus the particles follow the air flow due to diffusion charging. As particles approach the first discharge electrode, there is an increase in the particle's field charging since it has the greatest rate of charging, causing a fast deflection linked to the Coulomb force (Figure 12a).

When the particles are smaller (r_p = 0.2–2 µm), the drag force exerted by the airflow counteracts the Coulomb force. Consequently, the particle followed the gas flow. Upon approaching the right electrode ($0.7 < x < 0.9$ m), the particles deflect in the y direction (see Figure 12b and c).

With small particles (r_p = 0.1–0.5 µm), the high field intensity area is reduced, and the time deflection is lagged. Eventually, as the particle stream deflects, it escapes the electrostatic field or reaches the collecting plate. The smaller nanoparticle's radius (r_p = 0.01 µm = 10 nm) is near to the average molecular free path, and the collision in the air became discontinuous. Consequently, the drag force of the air is reduced, and the particle continues in its original direction (see Figure 12d).

Different angles of attack are shown in trajectories, corresponding to different collection efficiency. The smallest angle occurs at (r_p = 0.2 µm), and it increases away from this size. Due to reduced interphase drag and the effect of diffusion charging, particles smaller than 0.1 µm radius have an increased collection efficiency since the size of particles compared to the mean of molecular free path.

In Figure 13, six types of collecting electrodes in the ESP are used to show dust particle motion trajectories (2 µm). In ESP, particles reach the collecting plate at a 2×10^3 m/s for

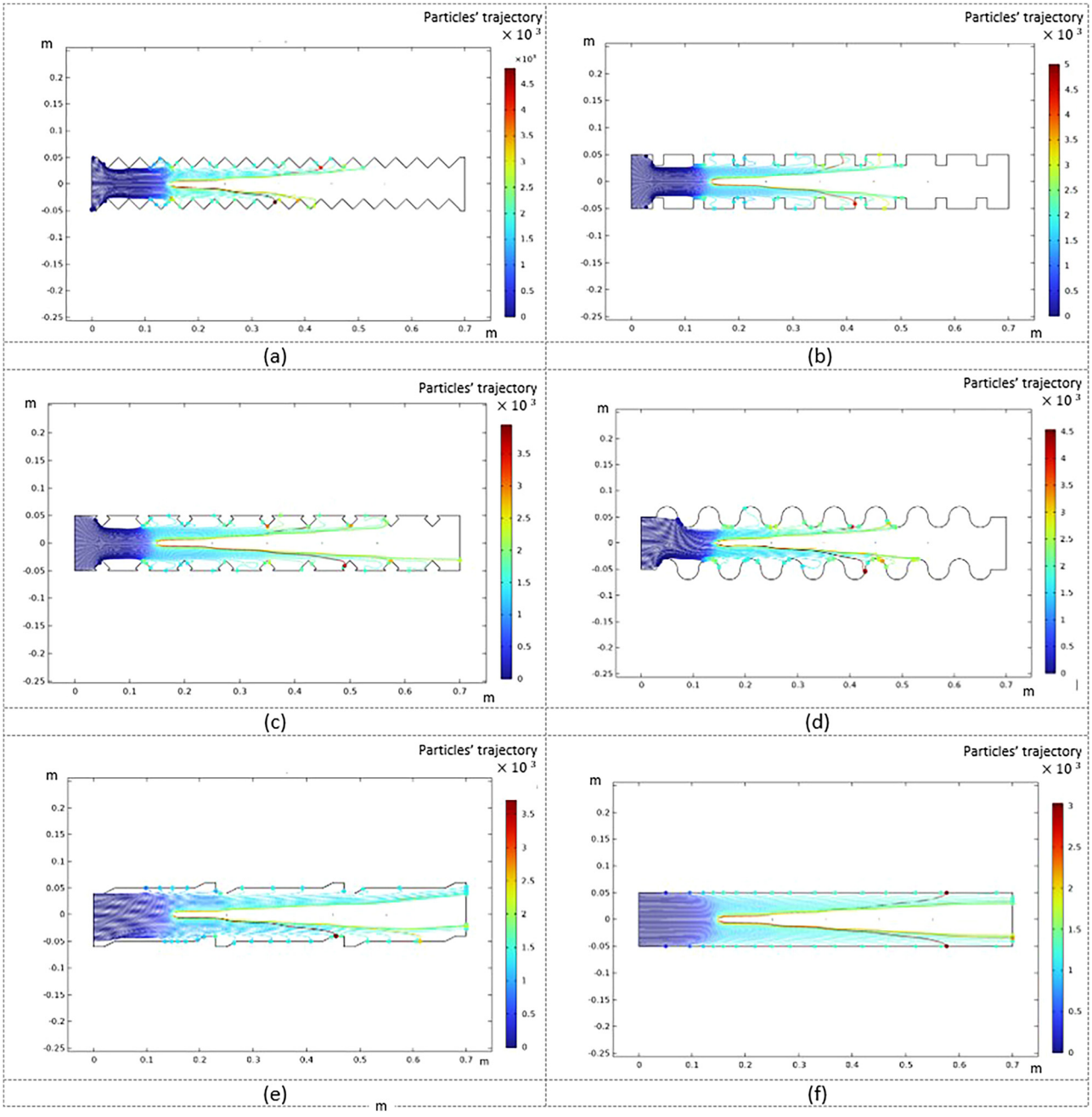

Figure 13: The dust particles trajectories in ESP (a) triangular plates, (b) crenulated plates, (c) corrugated-plates, (d) C-type plates, (e) BE-type plates and (f) flat plates collecting electrode, $r_p = 2$ μm.

flat plates, compared to 1.5×10^3 m/s for the particles near the other types of collecting plates. The flow field changes in proximity to the collecting plate produces the vortex of velocity and the trajectory of particles is whirling with triangular, crenulated, corrugated, C-type, and BE-type plates. Consequently, the particle trapping potential is increased since the velocity of particles decreases.

5.7 Particle migration

Figure 14 illustrates the distribution of the particle migration velocity with particle radius. When the particle radius is reduced from 10 μm to 1 μm, migration velocity decreases. When particle size varies from 0.1 to 1 μm, a small migration velocity is observed, due to a decrease in particle charge.

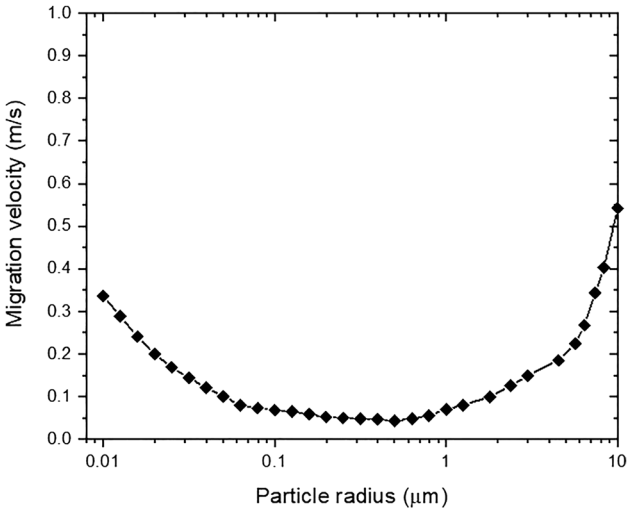

Figure 14: Particle migration velocities for different size particles.

When the size of particle is close to the average free path of the molecules (0.01–0.1 μm), the drag force influence on the particles decreased since the Cunningham correction and space charge particles are affected by corona suppression. Furthermore, with the reduce in drag force (<0.1 μm) and due to the reduction in particle size, the migration velocity of particles at 0.01 μm increased by 21 %.

5.8 Collection efficiency

As illustrated in Figure 15, the particle efficiency collection changes with particle size. A U-shape curve represents the overall trend of collection efficiency based on three level of particle size areas: (1) when particles are large (>1 μm), and because of their charging capacity and relatively low drag force, they are well captured, (2) middle-sized particles (between 0.1 and 1 μm) are not well collected, with a minimum around 0.2 μm in size. (3) Smaller particles (<0.1 μm) are captured due to the Cunningham correction factor, which counteracts the viscosity effect.

In hence, collection efficiency is greater at the extremes of particle dimensions. Smaller particles are more efficiently collected due to their lower drag force, while larger particles are more efficiently collected due to their greater electric charge. There is a maximum drag force between these two extremes, which results in a minimum collection efficiency (see Figure 15a).

As shown in Figure 15b, when five electrode discharges are used, the dust removal efficiency of ESP is greatest. Dust removal efficiency will be decreased if there are fewer or more discharged electrodes. Increasing the number of discharges from 5 to 6 can partially neutralize the negative effects of electrostatic shielding. Additionally, increased voltage reduces electrostatic shielding and increases particle discharge, improving collection efficiency.

Figure 16a illustrates the particle size function of ESP collection efficiency with five types of collecting electrodes. As observed, the triangular plate has the greatest collection efficiency of different particle sizes. It is found that the ESP with triangle plates (TP) has a 16 % higher efficiency for 10 μm particles as compared with the flat plates (FP) and the improved collection efficiency for smaller particles is slightly higher than larger particles.

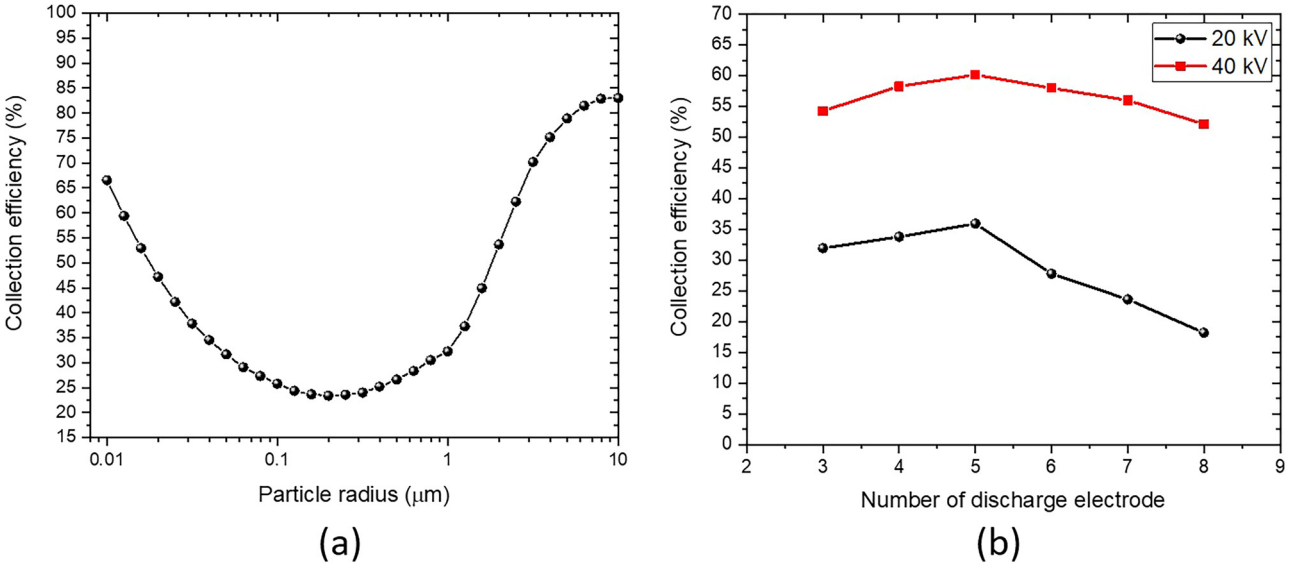

Figure 15: Distribution of particle collection efficiencies (a) for different size particles and (b) as function of number of discharge electrode for two applied voltages.

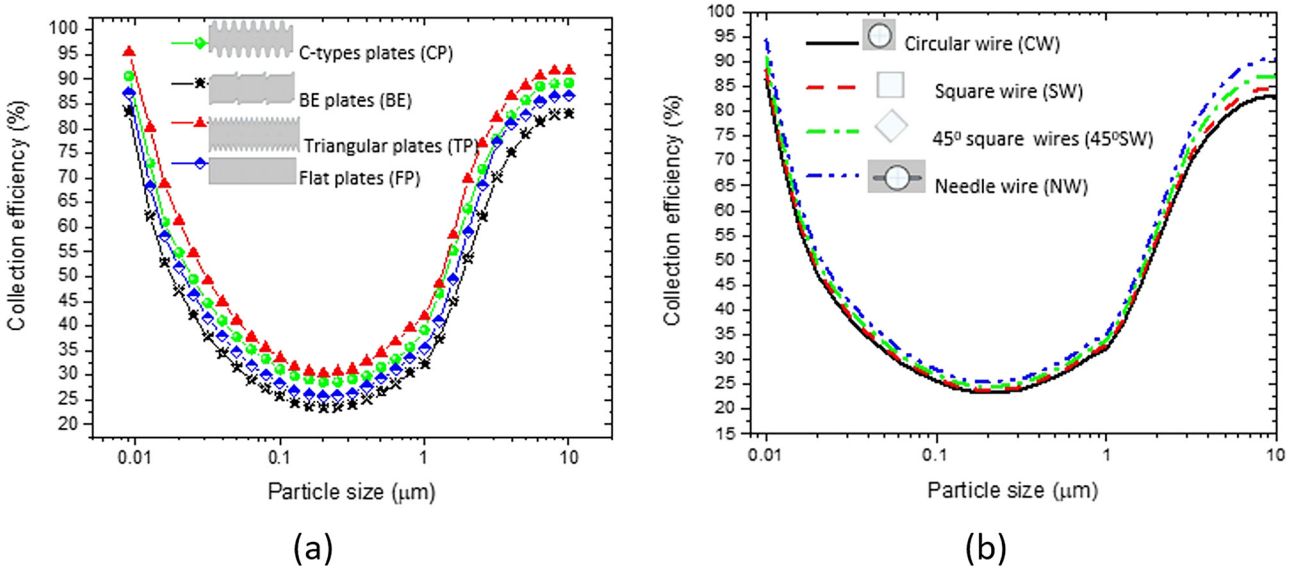

Figure 16: Particle collection efficiency with different particle size in the ESP (a) for FP and BE collecting electrode with circular corona wire and (b) for four types of discharge wire electrodes with FP collecting plates.

In particle capture, BE and C-type plates are more efficient than (FP) plates, but they are less effective than triangular plates due to the lower current density of FP plates than BE and C-type plates as the applied voltage increases. The particles charge more when using BE and C-type plates as applied voltage increases [38].

In Figure 16b, the efficiency of particle collection is shown for a variety of particle sizes and electrode wires. The needle wire (NW) is 4 % higher than the circular wire (CW) in the lowest case. Compared to circular discharge wire, the square wire (45° SW) is still in second place and slightly more efficient (about 2 %) in four cases. In comparison with the types of wire electrodes tested, needle wires achieved the highest efficiency because the lower spacing electrode provides greater efficiencies and greater increase in the total current when compared to wire electrode keeping larger space between wire electrodes [39].

The particle migration speed for different types of collection plates is shown in Figure 17a. The larger particle size radius (greater than 5 μm) has the highest migration

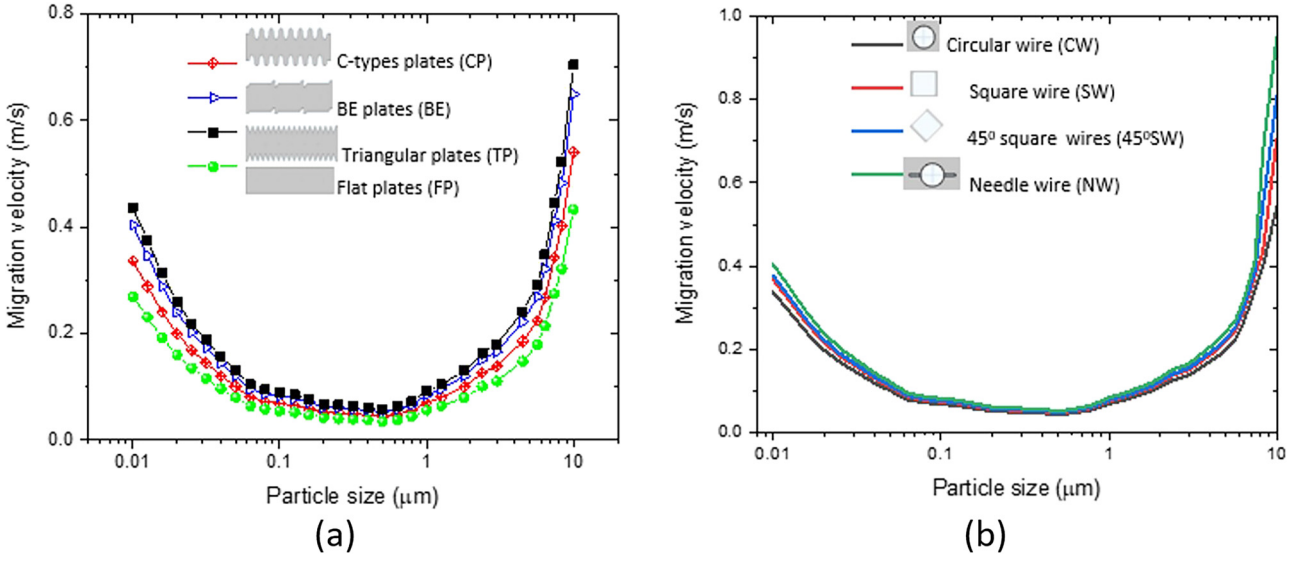

Figure 17: Particle Migration velocities with different particle size in the ESP (a) for FP and BE collecting electrode with circular corona wire and (b) for four types of discharge electrodes with FP collecting plates.

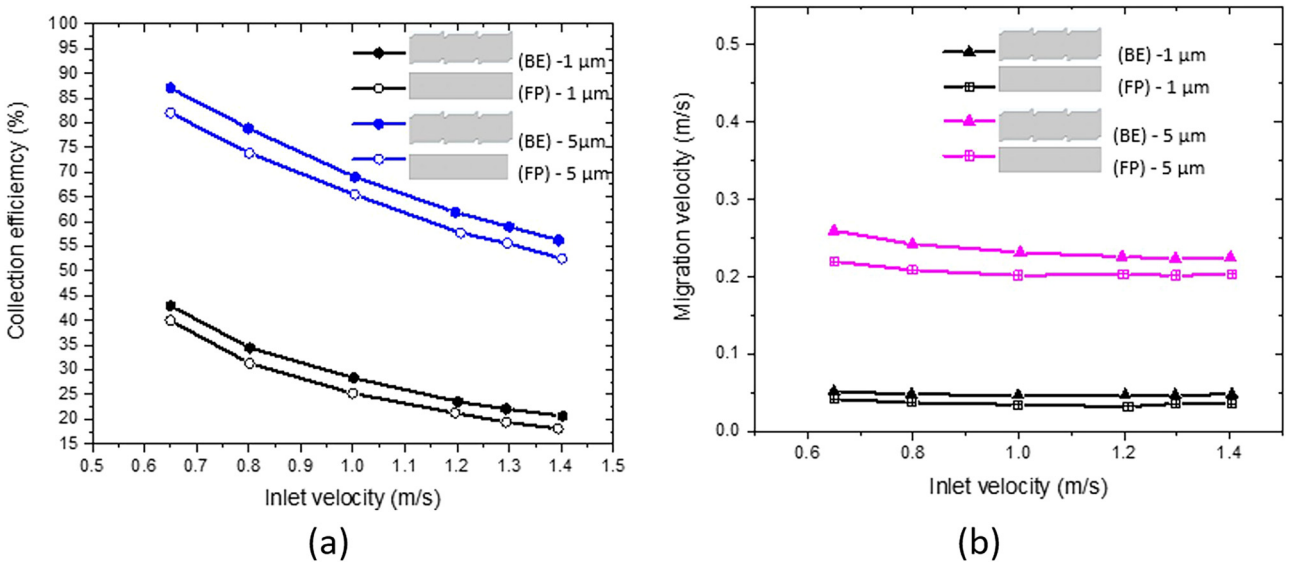

Figure 18: Distribution of dust particles (a) efficiency and (b) migration velocities versus inlet air flow velocities in flat and BE-type collecting plates with two particle's radius 1 and 5 µm.

velocity when compared to smaller particles using triangular plates. Compared to C-type and FP plates, the BE plate achieves a higher migration velocity [40].

In addition, the particle migration velocity in Figure 17b is influenced by various shapes of discharge electrode, with the same particle size. Particle migration velocity follows a similar trend as particle collection efficiency. It is shown that particle migration velocity increases more significantly for the NW electrode wire when radius particle size exceeds 2 µm, while between the NW and other electrodes ($r_p = 10$ µm), a maximum difference (0.1 m/s) is obtained. Based on this result, various discharge geometries play a crucial role in simulating ESP removal capacity. Consequently, comparatively to other electrode configurations, there is a significant improvement in performance using NW electrode with the FP collecting plate [41].

Figure 18a shows the efficiencies of particle collection for different inlet velocities illustrating the electrode configuration effect. At 1 and 5 µm particle sizes, a decrease in inlet velocity results in a decrease in the collection efficiency because particles have shorter residence times, smaller specific collection areas and insufficient charge [42].

In contrast, the inlet velocity has a smaller effect on particle migration velocity. Increasing the inlet speed from 0.8 to 1.4 m/s, almost has no effect on the particles of 1 µm. Migration velocity of 5 µm particles decreases since large particles have a high charge capacity.

Furthermore, reduced inlet velocity implies a higher residence time, which may result in a fast charge. Collection efficiency is affected by various electrode plate combinations with varying inlet velocities. Be wire electrode configurations show better collection efficiency and migration velocity when inlet velocity decreases for 1 and 5 µm particle sizes [43].

The migration velocity of particles at different inlet velocities is shown in Figure 18b. 1 µm seems to be almost unaffected. Because large particles have a high charge capacity, the migration velocity of 5 µm particles has slightly decreased since the inlet velocity increasing from 0.8 to 1.4 m/s. A low inlet velocity may also result in a longer residence time, resulting in a fast charge. A significant improvement in removal efficiency is achieved by reducing residence times of ionization, collection, and charging zones simultaneously by increasing the inlet velocity. Therefore, air flow is a key parameter that is a compromise between geometric dimensions (cross section, collector length) and performance [44].

The simulation results are shown in Figure 19 for three different temperatures. Fine particle collection efficiency and power consumption are significantly affected by temperature. The collection efficiency using particle sizes in the entire range is strongly influenced by temperature. By lowering the temperature from 400 to 450 K, the efficiency of the collection increases by 4 %. From 450 to 323 K, the collection efficiency increases by 40 %. The lower temperature range seems to be more effective for collection of dust particles [45]. Temperature has a greater effect on power consumption per unit area of a plate as follows ($J^* V_a$). If the temperature is reduced from 450 K to 323 K, the electrical power consumption increases by an order of magnitude.

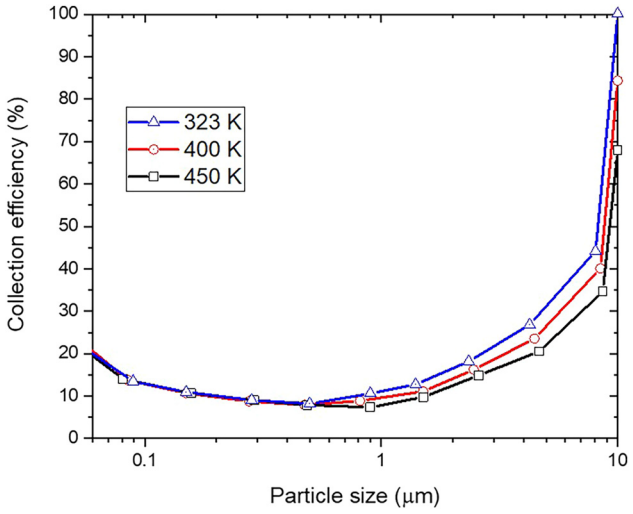

Figure 19: Particle collection efficiencies versus particle size at three values of temperature.

Therefore, increased power consumption is required to gain collection efficiency at lower temperature [46].

6 Conclusions

A multi-physical analysis of the ESPs characteristics used for indoor air cleaning from dust particles is investigated. Specifically, the paper discusses optimizing operation of electrostatic gas cleaning devices under actual industrial conditions under the range of 0.01–5 m dust precipitation and higher collection efficiency.

The numerical results of current voltage show a satisfactory agreement with experimental measurements, indicating the accuracy and the stability of the numerical model performed using COMSOL Multiphysics software. At first, it was shown that electrostatic processes can significantly improve the removal of dust particles for all size particles. With smaller inlet velocity of ESP, symmetric vortex structure around the discharge wires is observed because of ionic wind effect. While increasing inlet velocity weakens the ionic wind effect on flow patterns. Indeed, particle efficiency decreases with increasing air flow velocity and a speed of 1 m/s would be suitable.

Secondly, geometric parameters showed a synergistic effect on particle removal that led to higher overall and fractional efficiency. The use of uneven collecting plates reduces air pollution and improves ultrafine particles removal. The flow field near C-type, triangular, crenelated and corrugated collecting plates generate vortex causing particles to fly in a whirling motion. For ultrafine polluted particles, the triangular collecting electrode has the greatest collection efficiency.

With rising radius of the active electrode, the electric field, the applied potential, and the current density increase. In addition, as electrode radius increased, the speed difference between upstream and downstream flow of the wire increased, rising the effect of ionic wind on gas flow. Thus, increasing the electrode size enhances efficiency of the ESP.

Further, Increasing the number of needle electrode wires, wire diameters and wire to wire spacing improve ESP's collection of polluted particles efficiency. The multiwire single stage ESP has an optimum applied voltage of 40 kV and five number discharge electrodes.

Moreover, the agglomeration of particles in their entire aerodynamic size range has been discussed as a method to improve particle collection or filtration. All geometries and conditions showed lower fractional efficiency and migration velocity for the most penetrating particles (0.1–0.5 μm), while higher collection efficiency is deduced for ultrafine particles.

Consequently, multiwire single stage ESP show a higher efficiency in the removal of submicron dust particles from indoor environment with an optimum applied voltage of 40 kV and five number discharge electrodes.

Funding information: This research was funded by the Deanship of Scientific Research and Libraries at Princess Nourah bint Abdulrahman University, through the Research Funding Program, Grant No. (FRP-1445-5).

Author contributions: Samira Elaissi, Norah A.M. Alsaif, Eman M. Moneer and Soumaya Gouadria– methodology, writing, supervision, project management, supervision and revising the data. All authors have accepted responsibility for the entire content of this manuscript and approved its submission.

Conflict of interest: The authors state no conflict of interest.

Data availability statement: All data generated or analyzed during this study are included in this published article.

References

1. Garcia A, Santa-Helena E, Falco AD, Ribeiro JDP, Gioda A, Gioda CR. Toxicological effects of fine particulate matter (PM2.5): health risks and associated systemic injuries—systematic review. Water Air Soil Pollut 2023;234:346.
2. Mannerström M, Dvorakova M, Svobodova L, Rucki M, Kotal F, Vavrouš A, et al. New approach methods for assessing indoor air toxicity Current Research in Toxicology. Cur Res Toxicol 2022;3:100090.
3. Kong X, Guo C, Lin Z, Duan S, He J, Ren Y, et al. Experimental study on the control effect of different ventilation systems on fine

particles in a simulated hospital ward. Sustain Cities Soc 2021;73:103102.
4. Buggisch JR, Gohler D, Pape AL, Roger S, Ouaissi M, Stintz M, et al. Experimental model to test electrostatic precipitation technology in the COVID-19 era: a pilot study. J Am Coll Surgeons 2020;231:704—12.
5. Jeong SB, Shin JH, Kim SW, Seo SC, Jung JH. Performance evaluation of an electrostatic precipitator with a copper plate using an aerosolized SARS-CoV-2 surrogate (bacteriophage phi 6). Environ Technol Innov 2023;30:103124.
6. Shetty SS, Deepthi D, Harshitha S, Sonkusare S, Naik PB, Kumari S, et al. Environmental pollutants and their effects on human health. Heliyon 2023;9:19496.
7. Zuraimi MS, Nilsson GJ, Magee RJ. Removing indoor particles using portable air cleaners: implications for residential infection transmission. Build Environ 2011;46:2512—19.
8. De Oliveira AE, Guerra VG. Electrostatic precipitation of nanoparticles and submicron particles: review of technological strategies. Process Saf Environ Prot 2021;153:422—38.
9. Li Z, Liu Y, Xing Y, Tran TMP, Le TC, Tsai CJ. Novel wire-on-plate electrostatic precipitator WOP-EP; for controlling fine particle and nanoparticle pollution. Environ Sci Technol 2015;49:8683—90.
10. Kim M, Lim GT, Kim YJ, Han B, Woo C, Kim HJ. A novel electrostatic precipitator-type small air purifier with a carbon fiber ionizer and an activated carbon fiber filter. J Aerosol Sci 2018;117:63—73.
11. Sung JH, Kim M, Kim YJ, Han B, Hong KJ, Kim HJ. Ultrafine particle cleaning performance of an ion spray electrostatic air cleaner emitting zero ozone with diffusion charging by carbon fiber. Build Environ 2019;166:106422.
12. El-Sapa S, Alotaibi MA. Slip-driven interaction of dual spheres in couple stress fluids within a permeable medium. Mathematics 2025;13:2065.
13. Alotaibi MA, Algatheem AM, El—Sapa S. Magneto-slip interaction in the migration of two rigid spheres in infinite couple stress fluid. Chin J Phys 2025;95:173—89.
14. Anagnostopoulos J, Bergeles G. Corona discharge simulation in wire-duct electrostatic precipitator. J Electrostat 2002;54: 129—47.
15. Liu Y, Hu B, Zhou L, Jiang Y, Yang L. Improving the removal of fine particles with an electrostatic precipitator by chemical agglomeration. Energ Fuel 2016;30:8441—7.
16. Al-Hanaya A, El-Sapa S. Impact of permeability and fluid parameters in couple stress media on rotating eccentric spheres. Open Phys 2024;22:20240112.
17. El-Sapa S, Alotaibi MA. Migration of two rigid spheres translating within an infinite couple stress fluid under the impact of magnetic field. Open Phys 2024;22:20240085.
18. Yang Z, Zheng C, Liu S, Guo Y, Liang C, Zhang X, et al. Insights into the role of particle space charge effects in particle precipitation processes in electrostatic precipitator. Powder Technol 2018;339:606—14.
19. Chen B, Li H, He Y, Liu B, Zhang L. Study on performance of electrostatic precipitator under multi-physics coupling. Environ Sci Pollut R 2019;26:35023—33.
20. COMSOL Multiphysics® v51 wwwcomsolcom COMSOL AB, Stockholm, Sweden.
21. Guo B, Yu A, Guo J. Numerical modelling of ESP for design optimization. Procedia Engineer 2015;102:1366—72.
22. Afshari A, Ekberg L, Forejt L, Mo J, Rahimi S, Siegel J, et al. Electrostatic precipitators as an indoor air cleaner—A literature review. Sustainability 2020;12:8774.
23. Cornette JFP, Dyakov IV, Plissart P, Bram S, Blondeau J. In-situ evaluation of a commercial electrostatic precipitator integrated in a small-scale wood chip boiler. J Electrostat 2024;128:103897.
24. Wang X, Su H, Wang B, Tao J. Numerical simulation of spiked electrode electrostatic precipitator. J Electrostat 2024;132:103987.
25. Kim SH, Lee KW. Experimental study of electrostatic precipitator performance and comparison with existing theoretical prediction models. J Electrostat 1999;48:3—25.
26. Chen L, Gonze E, Ondarts M, Outin J, Gonthier Y. Electrostatic precipitator for fine and ultrafine particle removal from indoor air environments. Sep Purif Technol 2020;247:116964.
27. Chen YT, Lu CL, Lu SJ, Lee DS. Electrostatic precipitator design optimization for the removal of aerosol and airborne viruses. Sustainability-Basel 2023;15:8432.
28. Zheng C, Zhang X, Yang Z, Liang C, Guo Y, Wang Y, et al. Numerical simulation of Corona discharge and particle transport behavior with the particle space charge effect. J Aerosol Sci 2018;118:22—33.
29. Adamiak K. Numerical models in simulating wire-plate electrostatic precipitators: a review. J Electrostat 2013;71:673—80.
30. Lawless PA, Sparks LE. Modelling particulate charging in ESPs. IEEE T Ind Appl 1988;24:922—7.
31. Farnoosh N, Adamiak K, Peter GS. Castle numerical calculations of submicron particle removal in a spike-plate electrostatic precipitator. IEEE T Dielect El 2011;18:1439—52.
32. Feng Z, Long Z, Yu T. Filtration characteristics of fibrous filter following an electrostatic precipitator. J Electrostat 2016;83:52—62.
33. Khare M, Sinha M. Computer-aided simulation of efficiency of an electrostatic precipitator. Environ Int 1996;22:451—62.
34. Roginskaya L, Yalalova Z, Gorbunov A, Karimov R, Tereshkin V, Senyushkin N. Investigation of the high-voltage converter for powering electrostatic precipitators. E3S Web Conf 2023;446:02008.
35. Lee EM. Modelling of a novel large-scale electrohydrodynamic vortex flow induced by variation in current density for drag reduction with implication of electrostatic particle clustering. J Electrost 2024;128:103899.
36. Kim S, Hwang J. Numerical methodology to evaluate unipolar saturation current limit of DC Corona discharge in complex geometries. Sci Rep-UK 2022;12:14252.
37. Kasdi A. Computation and measurement of Corona current density and V-I characteristics in wires-to-plates electrostatic precipitator. J Electrostat 2016;81:1—8.
38. Asipuela A, Iváncsy T. Study and numerical simulation of the electrical properties of a duct-type electrostatic precipitator using seven circular Corona wires: a review periodica polytechnica. Electr Eng Comput Sci 2022;66:286—93.
39. Shen H, Yu W, Jia H, Kang Y. Electrohydrodynamic flows in electrostatic precipitator of five shaped collecting electrodes. J Electrostat 2018;95:61—70.
40. Lagarias JS. Discharge electrodes and electrostatic precipitators. Japca J AIR Waste Ma 1960;10:271—4.
41. Gao W, Wang Y, Zhang H, Guo B, Zheng C, Guo J, et al. Numerical simulation of particle migration in electrostatic precipitator with different electrode configurations. Powder Technol 2020;361:238—47.

42. Andrade RGSA, Guerra VG. Discharge electrode influence on electrostatic precipitation of nanoparticles. Powder Technol 2020;379:417—27.
43. Ji X, Huang J, Teng L, Li S, Li X, Cai W, et al. Advances in particulate matter filtration: materials, performance, and application. Green Energy Environ 2023;8:673—97.
44. Bologa AA, Seifert H, Paur HR, Hering W. Influence of gas composition on corona discharge characteristics in the high temperature/ high pressure electrostatic precipitator in Proceedings of 12th International Conference on Electrostatic Precipitation-ICESP'XII Nuremberg, Germany; 2011.
45. Guo BY, Yu AB, Guo J. Numerical modelling of electrostatic precipitation: effect of gas temperature. J Aerosol Sci 2014;77:102—15.
46. Shen H, Jia H, Kang Y. Electrical characteristics and electrohydrodynamic flows in electrostatic precipitator of six shaped discharge electrodes. J Appl Fluid Mech 2020;13: 1707—18.